

# On the possibility of radar echo detection of ultra-high energy cosmic ray- and neutrino-induced extensive air showers

Peter W. Gorham

*Jet Propulsion Laboratory, Calif. Inst. of Technology  
4800 Oak Grove, Drive, Pasadena, CA, 91109 USA*

## ABSTRACT

We revisit and extend the analysis supporting a 60 year-old suggestion that cosmic rays air showers resulting from primary particles with energies above  $10^{18}$  eV should be straightforward to detect with radar ranging techniques, where the radar echoes are produced by scattering from the column of ionized air produced by the shower. The idea has remained curiously untested since it was proposed, but if our analysis is correct, such techniques could provide a significant alternative approach to air shower detection in a standalone array with high duty cycle, and might provide highly complementary measurements of air showers detected in existing and planned ground arrays such as the Fly's Eye or the Auger Project. The method should be particularly sensitive to showers that are transverse to and relatively distant from the detector, and is thus effective in characterizing penetrating horizontal showers such as those that might be induced by ultra-high energy neutrino primaries.

*Subject headings:* Cosmic-rays, Cosmic-ray detectors, Extensive air showers, Neutrinos, Radar

## 1. Introduction

Extensive air showers (EAS) resulting from primary cosmic-ray particles of energies above 1 EeV ( $10^{18}$  eV) produce an ionization trail which is comparable to that of micro-meteors, which have been detected for many decades using radar methods (Lovell 1948; Greenhow, 1952; Hanbury Brown & Lovell 1962). In fact, Blackett & Lovell (1940) proposed that earlier detections of sporadic radio reflections at altitudes of 5-20 km from the troposphere and mesosphere (cf. Colwell & Friend 1936; Watson Watt et al. 1936a, 1936b, 1937; Appleton & Piddington 1938) might be attributed to cosmic ray EAS, although at the time both the energies and fluxes of such events were only crudely known. Later confirmation of the meteoric origin of higher altitude ionization trails may have contributed to a lack of follow-up on this prescient suggestion for the source of these low-altitude sporadics. The idea was re-examined in the early 1960's (Suga 1962) and a proposed experiment was described by Matano et al. (1968); however, no results from this test have appeared in the literature to date.

EAS ionization trails are now commonly detected by their air fluorescence emission at near-UV wavelengths (cf. Baltrusaitas et al. 1985). Future large EAS detector arrays such as the Auger project (Guérard et al. 1998) and the proposed space mission OWL/AirWatch<sup>1</sup> (Scarsi et al. 1999; Krizmanic et al. 1999) have made fluorescence detection of EAS a centerpiece of their approach, since it can provide information such as the position of the shower maximum and the total shower energy which can be difficult to pin down with particle detectors alone.

One of the most compelling reasons to extend the sensitivity of EAS detectors in this energy regime is the possibility that neutrinos of

energy  $\geq 10^{19}$  eV may be an important component of the primary particles (Capelle et al. 1999), contributing to the fluxes at these energies either directly or indirectly. Neutrinos and other highly penetrating particles will induce air showers that develop much deeper in the atmosphere than hadron-initiated showers. A unique signature of their presence would be the detection of highly inclined (near-horizontal) showers for which the point of maximum development is many radiation lengths deeper than is possible for a hadronic or electromagnetic shower. Thus any technique which (like the air fluorescence approach) has a particular sensitivity to showers of this type is of interest in addressing this problem.

To our knowledge no one has reported any studies the ionization trail of EAS using radar echo techniques, although as we will show here, the signals should be clearly detectable using standard radar methods. One reason for this may be the transient nature of the expected echoes; short duration transients are typically rejected by radar systems designed to detect or track targets where the reflectivity does not rapidly decay.

### **Ionization columns: meteors vs. EAS.**

Although there are many significant differences between the ionization caused by meteors and that of EAS, we can use the basic formalism developed for meteor study as a starting-point for analysis of EAS ionization. Meteor ionization trails are commonly parameterized in terms of their ionization line density  $\alpha$  (electrons  $\text{m}^{-1}$ ), a measure of the total ionization content divided by the length of the meteor track. Typical radar-detected meteors occur at heights of 80–120 km, and have line densities of  $\alpha = 10^{13}$  to  $10^{16}$   $\text{m}^{-1}$ . At the lowest detectable line densities, the incident meteor has a mass of  $\sim 1$   $\mu\text{g}$ , with a radius less than 100  $\mu\text{m}$ . At typical velocities of  $\geq 30$   $\text{km s}^{-1}$ , the implied kinetic energy of these meteor grains is 0.05 Joules or more, much of which goes into ionization of the air along its path.

A cosmic ray proton of energy  $10^{18}$  eV also

---

<sup>1</sup>Recently, the AirWatch program has evolved into a mission under consideration for the International Space Station, and has been renamed Extreme Universe Space Observatory (EUSO).

has a kinetic energy of order 0.1 J, and much of this energy also ultimately ends up in the form of ionization and excitation of atoms of the air along the path of the shower of charged particles that results from the proton's collision with nuclear hadrons. The primary differences between the meteor track and cosmic-ray-induced EAS are in the way the ionization column forms, and in the resulting ionization density profile.

For the meteor, ablation of material from its surface yields atoms with kinetic energies of  $10^2 - 10^3$  eV, which ionize air molecules by direct collision with a mean free path of several cm. This produces an ionization column with an approximately uniform distribution of radial density, and an initial radius of 2-10 m. The density then evolves with time due to diffusion, convective processes, bulk motions of the air, and the Lorentz forces of the ambient electric and geomagnetic fields. Electron attachment and recombination eventually complete the process of dissipating the ionization column. At radar frequencies in the HF to lower VHF range (10-100 MHz), echoes from typical meteors may be detectable for several seconds after the meteor is gone.

The ionization in an EAS, in contrast, is not produced by a single body, but rather by the collective effects of the disk highly energetic particles (mostly electrons and positrons) that make up the body of the shower. Because the lateral distribution of these particles spreads out as the shower progresses, the ionization column is formed with a different initial distribution than that of a meteor, reflecting the evolution of the cross-sectional charged particle density. In addition, since the shower propagates essentially at the speed of light, it appears almost instantaneously compared to even the fastest meteors at  $\sim 100 \text{ km s}^{-1}$ .

An important measure of the transverse charged particle distribution in an EAS is the Moliere radius  $r_m$  within which of order 90% of the charged particles can be found. For air at sea level,

$r_m \simeq 70$  m, but it is important to note that within  $r_m$  the radial distribution is a power law, and most showers retain a tight core of particles of diameter several m or less which may look much like the column initially produced by a meteor. In fact, of order 10% of the total number of electrons in an EAS are likely to be found within a radius of  $\simeq r_m/20$ , comprising much less than 1% of the area of the Moliere disk.

**Lightning ionization columns.** Lightning discharges also produce intensely ionized regions which have also been the subject of many radar studies since the early 1950's (Ligda 1950, 1956; Miles 1952). Ionization charge densities produced by lightning are many orders of magnitude higher than those produced by either EAS or small meteors, and the plasma channels produced by lightning are also of much smaller diameter than either meteor or EAS ionization columns. However they do occasionally occur in clustered networks with transverse scales comparable to those of EAS and meteors, and at altitudes that overlap the altitudes of EAS maxima. Thus they can provide examples of radar targets with features that are in some ways relevant to our discussion.

In the following section we present the concept of the radar cross section and outline specific cases relevant to EAS ionization columns. Section 3 develops a semi-analytical method for determining the ionization densities for a given air shower energy and altitude, and discusses some issues related to the evolution of the electron density. Section 4 then makes estimates of the radar echo power based on the formalism developed in the previous two sections. Section 5 concludes the paper with a discussion of some applications to specific experimental conditions.

## 2. Radar detection of ionization columns

For radar detection of the columns that result from meteors, EAS events, or lightning, there are two regimes to consider, depending on the plasma frequency  $\nu_p$  of the ionized region:

$$\nu_p = \sqrt{(n_e e^2 / \pi m_e)} \simeq 8.98 \times 10^3 \sqrt{n_e} \text{ Hz} \quad (1)$$

where  $n_e$  is the electron density in  $\text{cm}^{-3}$ . These two regimes are known in as the under- and over-dense regimes, respectively, and traditionally (in the meteor radar literature) are divided at the line density of  $\alpha \simeq 10^{14} \text{ m}^{-1}$ . However, because of the significant differences in the radial distribution of the electrons in EAS ionization compared to that of meteors, we distinguish them only on the basis of the ratio of radar frequency to plasma frequency, a distinction that is also common to radar lightning measurements. Thus we will consider the over-dense portion of an ionization column to be that region where the electron density is high enough that the plasma frequency exceeds the radar frequency, and the radar cannot penetrate it and is reflected. Underdense columns are those which have electron densities such that the local plasma frequency is below the frequency of the incoming radar, which can therefore penetrate the ionized region.<sup>2</sup>

Radar targets are most commonly described in terms of their effective radar cross section (RCS), a measure of the equivalent physical area of an ideal scattering surface. Here we will develop concepts useful to understanding the RCS characteristic to ionization columns, to prepare for later estimation of the expected radar return power from EAS-induced ionization.

<sup>2</sup>We stress here that underdense ionization columns may still produce a large radar return, for although the incident radio waves penetrate the column, the scattering may still be largely coherent, yielding a return power that scales quadratically with the electron density. This feature is of particular importance in determining radar's ability to provide estimates of the shower electron density and thus ultimately the energy of the primary particle.

In the following subsections we introduce general formulas for the RCS for both over- and under-dense cases. An additional distinction is also useful in each case: the long wavelength, or *Rayleigh* regime involves targets with characteristic dimensions smaller than the radar wavelength used; and the short wavelength, or *optical* regime involves cases where the characteristic target size is much larger than the radar wavelength.

### 2.1. Overdense ionization columns

When the electron density  $n_e(r_c)$  is high enough to produce a surface where the plasma frequency exceeds the frequency of the incident radiation at some critical radius  $r_c$  from the track, the resulting index of refraction becomes imaginary, and total external reflection of the radiation occurs. Under these conditions the surface at  $r_c$  can be treated to first order as a metal cylinder, and the RCS is accordingly greatly enhanced.

#### 2.1.1. Overdense columns: Rayleigh regime

When  $r_c \ll \lambda$ , the cylindrical region of reflecting plasma can be approximated as a thin wire. As we will show later when we develop an estimate of the ionization density for EAS, this is the case that will be most relevant to low-frequency radar echoes from EAS. In this case the maximum of the RCS, which occurs for normal incidence, can be approximated as (Crispin & Maffett 1965):

$$\sigma_{b,max}^{od} \simeq \frac{\pi L^2 \cos^4 \phi}{\left(\frac{\pi}{2}\right)^2 + (\ln[\lambda/(1.78\pi r_c)])^2} \quad (2)$$

where  $\phi$  the angle of linear polarization with respect to the axis of the wire. The behavior of  $\sigma_b$  at angles other than normal incidence is given by:

$$\sigma_b^{od}(\theta) \simeq \frac{\lambda^2 \tan^2 \theta \cos^4 \phi}{16\pi \left[ \left(\frac{\pi}{2}\right)^2 + (\ln[\lambda/(1.78\pi r_c \sin \theta)])^2 \right]} \quad (3)$$

where  $\theta$  is the angle as measured from the axis of the wire (or EAS in our case). This approximation is valid in the range  $60^\circ \leq \theta \leq 120^\circ$ , but underestimates the cross section at angles closer to the axis of the wire, due to what are known as *traveling wave* effects, which produce large cross sections near the axis, in some cases comparable to that at normal incidence (Medgyeshi-Mitschang & Putnam 1985), and significantly broader in angular range. However, the treatment of such effects is very complex and beyond our scope at present.

### 2.1.2. Overdense columns: Optical regime

When  $r_c \gg \lambda$ , the reflection from the critical surface becomes almost entirely specular, and for normal incidence we have (Kraus 1988)

$$\sigma_{b,max} = \frac{2\pi r_c L^2}{\lambda} \quad (4)$$

where  $\sigma_{b,max}$  denotes the maximum value of the RCS, and  $L$  is the length of the cylindrical reflecting surface. Radar cross sections for metal cylinders have been studied in detail (cf. Medgyeshi-Mitschang & Putnam 1985) and are complicated functions of angle, with resonances and nulls that depend strongly on the length and other factors. As we shall establish below, EAS ionization columns will generally not fall into the optical regime for the overdense case, except at very high EAS energies and very low radar frequencies. For this reason we do not treat these effects further here.

## 2.2. Underdense ionization columns

For radar frequencies well above the plasma frequency  $\nu_p$ , the radiation penetrates the entire ionization column, and the electrons within the ionization column scatter independently according to the Thomson cross section

$$\sigma_T = \frac{8\pi}{3} \left( \frac{e^2}{m_e c^2} \right)^2 = 6.65 \times 10^{-29} \text{m}^2. \quad (5)$$

The total effective radar backscatter cross section  $\sigma_b$  will then depend on the individual phase factors of each of the scattering electrons.

### 2.2.1. Underdense columns: Rayleigh regime

For  $r_m \ll \lambda$ , and angles that are nearly perpendicular to the track, all of the electrons scatter coherently over a longitudinal region of the track  $L_F = \sqrt{\lambda R/2}$  where  $R$  is the perpendicular distance to the track and  $\lambda$  the radar wavelength (Hanbury-Brown & Lovell 1962). This region of the track is known as the first Fresnel zone of the track, and the total radar backscatter cross section then becomes

$$\sigma_b = N_e^2 \sigma_T, \quad (6)$$

where  $N_e = \alpha L_F = \alpha \sqrt{\lambda R/2}$  is the number of electrons within a single Fresnel zone along the track. The radar cross section depends of the square of the electron density because of the assumption of full coherence.

Except for radar frequencies  $f \ll 10$  MHz, most radar ranging of EAS ionization columns is not in the Rayleigh regime. However, the concept of the Fresnel zone, which establishes a characteristic length scale over the longitudinal extent of the track, will still be useful in what follows.

### 2.2.2. Underdense columns: Optical regime

For tracks where the radar frequency  $f > \nu_p$ , but  $r_m \geq \lambda/4$ , the assumption of coherent scattering is no longer satisfied, and the individual phase factors of the electrons must be included. For this case the effective RCS can be written (cf. Wehner 1987; also see appendix):

$$\sigma_b^{ud}(\mathbf{k}) = \left| \int n_e(\mathbf{r}) \sqrt{\sigma_T} e^{2i\mathbf{k}\cdot\mathbf{r}} d^3\mathbf{r} \right|^2 \quad (7)$$

where  $\mathbf{k}$  is the wave vector of the incident field ( $k = 2\pi/\lambda$ ),  $\mathbf{r}$  is the vector distance to the volume element at which the scattering takes place. Here we are neglecting refractive effects of the ionization column on the incident radiation, and

assuming that the incident and backscattered waves satisfy  $\mathbf{k} \cdot \mathbf{r} \simeq |kr|$ .

Note that the argument of the exponential here includes an extra factor of two to represent the two-way phase. This is due to the fact that as the scattered radiation returns on the same path as the incident radiation, it picks up an additional phase factor equal to that of the incoming radiation. The term  $n_e(\mathbf{r})\sqrt{\sigma_T} d^3r$  represents the differential contribution to the scattered electric field of a volume element of electrons which scatter coherently.

If we now write  $\mathbf{q} = 2\mathbf{k}$  then equation 7 becomes

$$\sigma_b^{ud}(\mathbf{q}) = \sigma_T \left| \int n_e(\mathbf{r}) e^{i\mathbf{q}\cdot\mathbf{r}} d^3\mathbf{r} \right|^2 \quad (8)$$

Equation 8 thus reduces the problem of estimating the effective cross section in the underdense case to that of calculating the Fourier transform (and the resulting power spectrum) of the electron number density distribution. In the appendix we describe the geometry more explicitly and show how this relation arises.

A broader implication of this result can be stated as follows: *A measurement of the complex amplitude of the radar echo from an EAS in the underdense case is proportional to a measurement of one Fourier component of the shower ionization profile.* This will be true even in the case of a bistatic radar (receiver location not coincident with transmitter) although there will be an additional coefficient to account for the bistatic cross section and its angular behavior.

### 3. EAS ionization densities

In the previous section we introduced the mechanisms for radar reflection from cylindrical plasma columns in two regimes of ionization density. Here we estimate the spatial distribution of the expected ionization from a high energy cosmic-ray air shower, which will then allow us to assess their effective radar cross section.

### 3.1. Longitudinal ionization

There are many years of development of the theory of EAS production. The most accurate treatments of the evolution of the electron density in the shower require numerical simulations, but there are a number of parameterizations available that yield results accurate enough for our needs. Here we use the analytical model due originally to Kamata & Nishimura (1958), and Greisen (1965), often referred to as the NKG approximation. In the NKG model the longitudinal (along-track) development of the shower at a depth  $d$  is parameterized by its *age*  $s$ :

$$s(d) = \frac{3d/X_0}{d/X_0 + 2 \ln(E/E_{crit})} \quad (9)$$

where  $E_{crit} = 86$  MeV for electrons in air, and  $X_0 = 36.7$  gm cm<sup>-2</sup> is the electron radiation length in air. The evolution of the total number of charged particles (virtually all electrons and positrons) with depth is then approximated by

$$N_e = \frac{0.31 \exp[(d/X_0)(1 - 1.5 \ln s)]}{\sqrt{\ln(E/E_{crit})}} \quad (10)$$

Although this approach does not account for any of the large fluctuations that are possible in high energy air showers, it describes the average behavior reasonably well.

### 3.2. Transverse ionization density

The transverse charged particle densities are described in a similar fashion, also parameterized by the age of the shower and the Moliere radius  $r_m$  (Bourdeau 1980):

$$\xi_e = K_N \left( \frac{r}{r_m s_m} \right)^{s-2} \left( 1 + \frac{r}{r_m s_m} \right)^{s-4.5} \quad (11)$$

where

$$K_N = \frac{N_e}{2\pi r_m^2 s_m^2} \frac{\Gamma(4.5 - s)}{\Gamma(s)\Gamma(4.5 - 2s)} \quad (12)$$

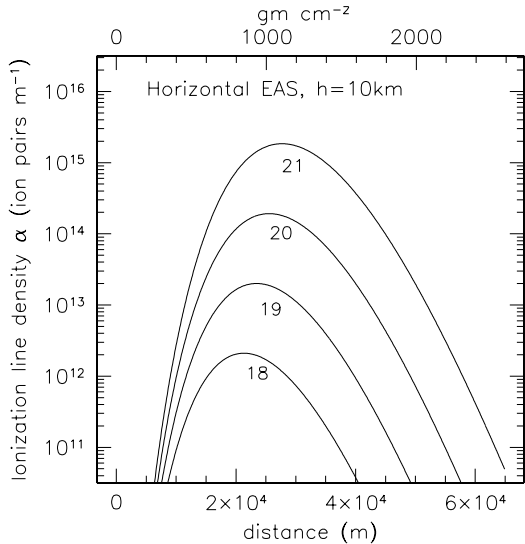


Fig. 1.— Electron ionization line density for 5 showers of energies in the  $10^{18}$  to  $10^{21}$  eV range. Such line densities are quite similar to those of radio meteors.

and  $\Gamma$  is the gamma function, and  $s_m = 0.78 - 0.21s$ . The Moliere radius for air is given by

$$r_m = 2.12 \times 10^5 \frac{X_0}{E_{crit} \rho} = 70 \left( \frac{\rho_0}{\rho} \right) \text{ m} \quad (13)$$

where  $\rho$  is the density of the air at the altitude under consideration, and  $\rho_0$  is the sea level density. The calculated density  $\xi_e$  is in units of charged particles per unit area, passing through a plane transverse to the shower axis at the given depth. Since the shower thickness is typically of order several meters or less over its length,  $\xi_e$  can be approximately equated with the number density in a slab transverse to the shower.

To convert these particle number densities to the resulting ionization density, we use the average value for electron energy loss given by  $E_{crit}/X_0 = 2.343 \text{ MeV gm}^{-1} \text{ cm}^{-2}$ , divided by the mean energy per ion-pair for air  $E_{ion} = 33.8 \text{ eV}$  (Segre 1977) which accounts for the inefficiency of ion-pair production. This procedure is similar to that used by the Fly's Eye (Baltru-

saitas et al. 1985) in estimating shower parameters based on fluorescence yield.

We note here that the NKG approach and subsequent modifications to it do not accurately account for the electron distribution at large radii from the core, and will in general underestimate the electron density beyond the Moliere radius. However, since the ionization density at large radii is low compared to the core, there is very little coherent contribution from these electrons, in spite of their large integrated number. Our results remain basically unchanged by this effect.

### 3.3. Numerical results

Fig. 1 shows curves of calculated ionization line densities for several EAS of different primary energies over the range of  $10^{18} - 10^{21}$  eV. The showers are assumed to be propagating horizontally at an altitude of 10 km, and the shower parameters are corrected for the lower air density at this altitude. The bottom axis shows the along-track distance corresponding to the depth shown along the top axis. As noted above, the line densities at these energies correspond to typical line densities of radio meteors, which are detected at heights of 80-120 km. However, the lateral distributions will be quite different as noted above. We note also that the showers are physically very long, with the region of shower maximum extending over many km of physical distance for most showers at these energies.

In Fig. 2 we show the effective line density as a function of the radius within which the electron density is integrated, for the inner 40 m radius for the same set of showers shown in Fig. 1. Here it is evident that the effective line densities of the inner  $\sim 10$  m radius core of the showers are about a factor of 10 lower than those which include all the electrons produced in the shower. However, this area corresponds to only 0.25% of the area of the Moliere disk ( $r_m \simeq 200$  m at 10 km), It is thus evident that the cores of the showers are highly concentrated in ionization density with respect to the bulk of the shower disk area.

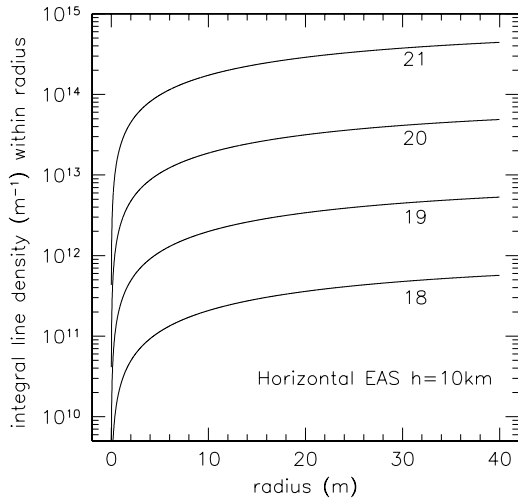


Fig. 2.— The effective line density of an EAS near its shower maximum as a function of the radius within which the electron density is integrated. It is evident that the effective line densities within radii of 10 m or so are about 10% of the total line densities shown in Fig. 1, and are still substantial.

In Fig. 3, we show the lateral ionization density distributions near shower maximum for the same four EAS presented in Fig. 1 (solid lines). Included also are curves of the effective plasma frequency corresponding to the density at each radial distance (dashed lines). Given the uncertainty in the accuracy of the analytical model for EAS development at very small core radii (cf.  $r < 20$  cm), the implied highest radar frequencies that will undergo total reflection are in the range of 10-50 MHz, with a strong dependence on the primary energy.

It is evident from Figures 2 and 3 that the cores of the showers are likely to be most important in determining the radar response, since the electron density is much higher near the core. In Fig. 4, we plot the core electron density again near shower maximum for a  $10^{20}$  eV horizontal shower, at a variety of different altitudes to

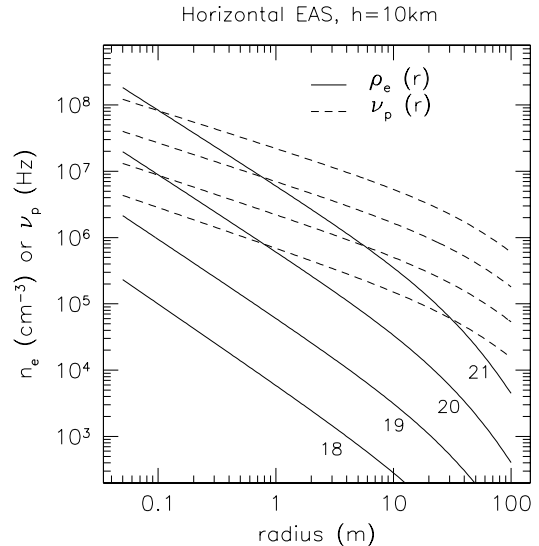


Fig. 3.— Radial dependence of the ionization density for the same showers presented in the previous figure. Also shown is the radial dependence of the plasma frequency for each case.

display the effects of the different atmospheric density. To first order the shape of the core is preserved with altitude, but the overall electron density decreases at higher altitudes because the production rate of ionization depends on the density of the air.

### 3.4. Duration of the radar echo

Before estimating the radar echo power, we first address the important topic of the expected lifetime of the free electrons in the ionization column. If EAS detection by radar is to be proven practical, it is first necessary to first establish that the ionization column can be treated as quasi-static over the timescale it might take to interrogate the shower with a radar pulse, either as a standalone system, or if a separate air shower detector provided the trigger.

As an example of the issue with respect to triggered operation, consider a large air shower array with radius 30 km. For typical electron-



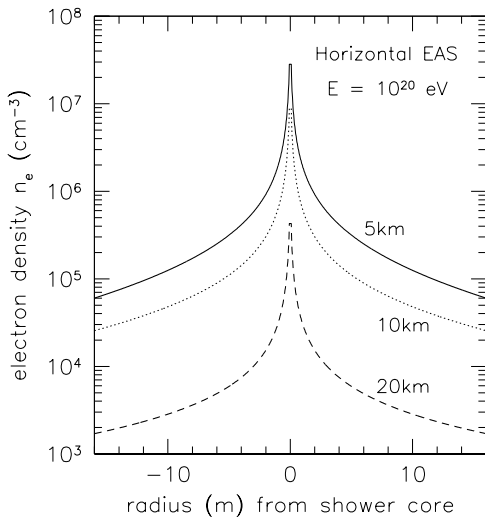


Fig. 4.— Radial profile of showers shown for the inner 40 m radii, plotted on a linear distance scale, for different shower altitudes, showing the effects of altitude for a set of horizontal showers.

ics used in such systems the trigger forms within several tens of  $\mu\text{s}$ . Round trip transit time to an EAS within  $\sim 30$  km requires another  $200 \mu\text{s}$ . Thus in this case we require EAS electrons to remain mostly free for of order  $250 \mu\text{s}$  or longer, if an external trigger is to be used to allow interrogation of a detected shower. In general, if the free electron lifetime is  $\tau_e$ , and the trigger formation and pulse initiation time is  $\tau_p$ , then the maximum range for a triggered system is

$$R_{tr} \leq c \frac{\tau_e - \tau_p}{2}. \quad (14)$$

If a radar detection system is operated in a standalone mode, the free electron lifetime will determine how often the detection volume must be pulsed in order to have a reasonable efficiency at detecting the EAS. In the limit where the free electron lifetime becomes so short that it is comparable to the pulse duration, then pulsed radar detection will become impractical. Other methods which use continuous-wave (CW) techniques

may still apply in this case; these will be discussed briefly in a later section.

There are a number of effects that cause the electron density to evolve with time:

1. Diffusion of the electrons through the ambient air, lowering their density and thus their net radar cross section;
2. Electronic recombination with ions;
3. Attachment of electrons to neutral molecules, or dissociative attachment to atoms;
4. Collisional detachment of previously attached electrons, which frees electrons that have been attached to atoms;

#### 3.4.1. Diffusion effects

Although the conditions of the atmosphere at the 80-120 km heights that meteor echoes are observed at are quite different from those at EAS heights, it is useful to preface our analysis with a discussion of the effects that determine the time scale for meteor echoes.

The duration of meteor radar echoes has been modelled and studied experimentally in detail for many decades (cf. Hanbury Brown & Lovell 1957; Kaiser 1968; Kaiser et al. 1969; Jones & Jones 1990; Jones 1991). The power of a meteor radar echo is found in the underdense regime to decay exponentially with a time constant  $\tau_m = \lambda^2 / (32\pi^2 D_i)$  where  $D_i$  is the ambipolar (or ion neutral) diffusion coefficient. At the altitudes that meteors are observed with radar,  $D_i \simeq 1 - 10 \text{ m}^2 \text{ s}^{-1}$ , and the typical decay times for underdense trails are thus several tens of ms for frequencies in the VHF regime.

To estimate diffusion effects at the lower altitudes of EAS ionization columns, we note that  $D_i \propto T\nu_i^{-1}$  where  $T$  is the kinetic temperature and  $\nu_i$  the collision frequency (cf. Buonsanto et al. 1997). Thus at 10 km altitude, the diffusion coefficient is much smaller,  $D_i \sim 5 \text{ cm}^2 \text{ s}^{-1}$ , due mainly to the much higher collision frequency

at lower altitudes. The implied time constant, assuming diffusion progresses in the same manner for EAS as for meteor ionization columns, is  $\tau_{eas} \simeq 60$  s for  $\lambda = 3$  m.

S-band radar echoes from lightning at altitudes of  $\sim 10$  km measured by Williams et al. (1984) were frequently found to persist for several hundred milliseconds. For a wavelength of 11 cm, the diffusion time constant at this altitude is 240 ms, which suggests that diffusion may be the dominant effect in the evolution of lightning radar cross section, at least at microwave frequencies. However, lightning ionization densities are estimated to be initially  $10^{13} - 10^{14}$   $\text{cm}^{-3}$ , with plasma frequencies  $10^3$  or more times higher than for EAS columns. Thus other effects relevant to the conditions of this much denser plasma may be important.

### 3.4.2. Attachment & Recombination

Since diffusion is less effective at dissipating the ionization column of an EAS than it is for a meteor, at least at VHF frequencies, we expect that attachment and recombination may play a more significant role. The recombination rate for atmospheric electrons is described by (cf. Thomas 1971):

$$\frac{dn_e}{dt} = N_e^0 - \alpha_e n_e^2 - \beta_e n_e \quad (15)$$

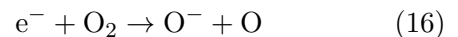
where  $N_e^0$ ,  $n_e$  are the initial and evolving electron density, respectively,  $\alpha_e$  is the electron-ion recombination coefficient (in units of  $\text{cm}^3 \text{s}^{-1}$ ),  $\beta_e$  and is the electron attachment rate ( $\text{s}^{-1}$ ). Here we have ignored terms in Thomas (1971) which relate to the presence of negative ions in the ionosphere since we are considering EAS within the troposphere where such ions are not prevalent.

The electronic recombination coefficient for hydrogenic atoms can be approximated by (Seaton 1959)

$$\alpha_e = 5.20 \times 10^{-14} Q^{1/2} \times (0.429 + 0.5 \ln Q + 0.469 Q^{-1/3}) \text{ cm}^3 \text{ s}^{-1}$$

where  $Q = 1.58 \times 10^5 / T_e$  and  $T_e$  is the electron kinetic temperature, with  $T_e \simeq 10^3 - 10^4$  K typical for ionization in this case. For air in the troposphere we thus expect  $\alpha_e \sim 10^{-12}$  to  $10^{-11}$   $\text{cm}^3 \text{s}^{-1}$ , and the implied recombination time for the highest electron densities we have considered is several minutes or more. Thus it is highly probable that the electrons will attach before recombining.<sup>3</sup>

Molecular oxygen is electronegative, forming ions with free electrons primarily through dissociative attachment, via the process



where the resulting oxygen ion and atom carry off the excess kinetic energy of the electron, and the electron affinity of  $\text{O}_2$  is of order 0.5 eV. Molecular nitrogen, in contrast, does not form attachments with electrons but can be more easily collisionally excited, and may play a role in mediating detachment processes in air.

Several studies of electron attachment in air using electron swarm techniques (see Gallagher et al. 1983 for a compilation) have indicated a much lower attachment rate than that which is expected from using the attachment coefficient for pure molecular oxygen reduced by the molar ratio in air (Moruzzi & Price 1974 & references therein). Measurements of the attachment coefficient are very sensitive to contamination by carbon dioxide, and  $\text{CO}_2$  was not removed from the samples in many early measurements. Although  $\text{CO}_2$  can be present in significant concentrations in the near sea level atmosphere, its average concentration in the atmosphere as a whole is 0.033%. Thus electron attachment rates for dry, high-altitude air must be determined with  $\text{CO}_2$  largely removed from typical air samples.

<sup>3</sup>We note that values for the total recombination coefficient of  $\alpha = 2 \times 10^{-7}$   $\text{cm}^3 \text{s}^{-1}$  are found in the D region of the ionosphere (Thomas 1971). Such a high value is likely to be due to the large variety of ion species present, which increases the total recombination cross section per electron.

Moruzzi & Price (1974), after carefully removing all CO<sub>2</sub> from their samples, confirmed earlier measurements in being unable to detect any attachment in pure dry air. This result was attributed to a competing process: rapid collisional detachment from N<sub>2</sub> interactions, yielding an effective attachment rate that was less than 10% of the ionization rate and thus too small to measure. Their limit on the effective attachment coefficient ( $\eta^*/N_m$ ) for pure air is

$$(\eta^*/N_m) \leq 3 \times 10^{-20} \text{ cm}^2. \quad (17)$$

where  $N_m$  is the number density of the attaching molecular species. The attachment rate  $\beta_e$  is related to the effective attachment coefficient through

$$\beta_e = (\eta^*/N_m(h))u_e N_m(h) \quad (18)$$

where  $u_e$  is the electron drift velocity. For a typical electron drift velocity of  $u_e = 2 \times 10^5 \text{ cm}^{-1} \text{ s}^{-1}$ , the limit on  $\eta$  gives  $\beta_e \leq 5.4 \times 10^4 \text{ s}^{-1}$ , implying that attachment dominates completely over recombination.

Figure 5 shows the behavior of the electron density for three different altitudes for a  $10^{19} \text{ eV}$  shower core region. Here we have plotted the electron density time evolution for both the case where the attachment rate is equal to the limit of Moruzzi & Price (1974), and one-tenth of the limit (dashed lines). It is evident that the expected electron lifetimes are at least 10-20  $\mu\text{s}$ , increasing slowly at the higher altitudes.

Although this estimate of the electron attachment lifetime is important from the point-of-view of evaluating whether there is sufficient time for triggered-interrogation of an EAS with radar, it is also important to establish an upper limit on the electron lifetime, both for purposes of evaluating the possibility of multiple-pulse interrogation of a shower, and for considerations of radar clutter from echoes of multiple showers for a radar system with very large range.

The lightning radar measurements noted above (Williams et al. 1984 & references therein) of-

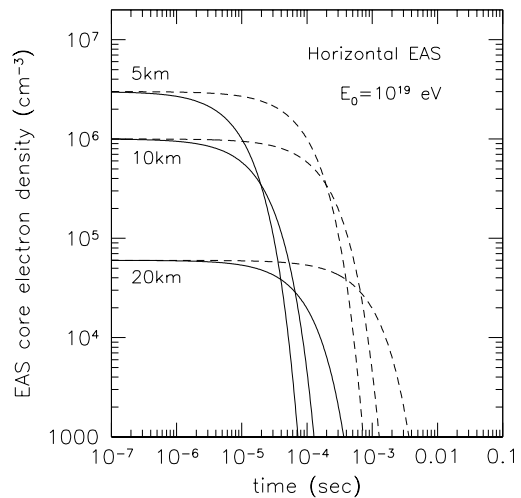


Fig. 5.— The evolution of the electron number density is shown for three  $10^{19} \text{ eV}$  EAS, at different altitudes. The solid lines correspond to the evolution for the present upper limit on the attachment rate, and the dashed lines to one-tenth of the upper limit.

ten found radar echo persistence of several hundred ms using repetitive radar pulses. However, the plasmas produced by lightning are extremely overdense and hot relative to those we are considering, and thermal detachment may play a significant role. In addition, the large amount of water vapor present in typical lightning radar measurements complicates any comparison with EAS in dry air. Thus comparison of radar echoes from lightning with those from EAS ionization must be done with caution.

An rough upper limit for the free electron lifetime can be obtained by considering the equilibrium level of free electron content of the mesosphere in the region of maximum cosmic ray ionization, peaking at about 12-14 km altitude. Here the dominant ionization is caused by low energy (several hundred GeV and above) cosmic ray air showers, which produce of order 30 ion pairs per  $\text{cm}^3$  per second (Rossi 1966; Gregory &

Clay 1982), roughly 15 times the sea level rate of ion production.

The DC conductivity of the atmosphere at 12 km is  $\sigma_0 \simeq 4 \times 10^{-13} \Omega^{-1}\text{m}^{-1}$  (Dolezalek 1982). The cosmic ray ionization at this altitude induces a tenuous plasma, with DC conductivity

$$\sigma_0 = 4\pi\epsilon_0 \frac{\pi\nu_p^2}{\nu_{en}} \quad (19)$$

where  $\epsilon_0$  is the dielectric permittivity constant, and the electron-neutral molecule collision frequency  $\nu_{en}$  can be written as

$$\nu_{en} \simeq 4 \times 10^{-10} \sqrt{T_e} N_m \quad (20)$$

where  $N_m$  is the molecule number density ( $\text{cm}^{-3}$ ) at the altitude considered. The electron temperature  $T_e$  is uncertain but likely to be in the range of 300-2000 K. At 12 km we thus expect  $\nu_{ei} \simeq 4 \times 10^{10} \text{ s}^{-1}$  for  $T_e = 300 \text{ K}$ .

Inverting equation 19 for the plasma frequency, which in turn depends on the equilibrium electron number density (equation 1), we find

$$n_e \simeq 35.5 \nu_{en} \sigma_0 \text{ cm}^{-3}. \quad (21)$$

For the values determined above we have  $n_e \leq 0.57 \text{ cm}^{-3}$  which implies a mean lifetime of less than 20 ms. The actual electron lifetime will be less than this since the detailed DC conductivity also includes contributions from ionic terms which we have neglected here. There will also be an altitude dependence on this upper limit since it depends on the collision frequency. In summary, we find that the available time for EAS interrogation by radar is bounded at 10 km altitude approximately by

$$20 \mu\text{s} \leq \tau_e \leq 20 \text{ ms} . \quad (22)$$

Thus, for the shortest values of  $\tau_e$ , triggered interrogation of air showers appears to be impractical except for ranges of a few km or less; for the largest possible values, ranges of hundreds to even a thousand km or more are not excluded

for higher altitude showers. In the latter case, no existing system can yet trigger on showers at these great distances, but planned space-based systems such as OWL/AirWatch will have such capability.

The  $\sim 20$  ms upper limit to the electron lifetime shows also that radar clutter from echoes of multiple showers should be completely negligible. For example, even assuming an energy threshold as low as  $10^{16}$  eV could be attained out to 10 km, the shower rate at this energy over this area is still only several events per second. Radar systems also generally allow range-gated triggers, and this can facilitate rejecting any nearby clutter from low-energy showers within a few km of the transmitter.

#### 4. Predicted radar return power from EAS

Having established that the duration of the EAS radar targets is likely to be sufficient for their detection, and introduced the radar cross sections expected, we now turn to estimation of the return power of the echo.

Radar return power  $P_r$  is described in terms of a model where the radiation is emitted from an antenna with peak transmitted power  $P_t$  and directivity gain  $G = 4\pi\Omega_A^{-1}$ , where  $\Omega_A$  is the solid angle of the main beam of the antenna. The radiation is assumed to then scatter from objects in the antenna beam and be re-radiated isotropically in the frame of the scatterer, producing a  $R^{-4}$  dependence in the returned power as a function of range  $R$ . Deviations from isotropic scattering are thus absorbed into the effective radar backscatter cross-section  $\sigma_b$ , which can be larger or smaller than the physical cross-section of the object. In addition any real transmitting and receiving system will have less than unity efficiency, which we designate here as  $\eta$ . The radar equation under these conditions is (cf. Skolnik 1990)

$$\frac{P_r}{P_t} = \sigma_b \eta \frac{G^2 \lambda^2}{(4\pi)^3 R^4} . \quad (23)$$

Here we are assuming that the transmitting and

receiving antennas are identical, and we are neglecting for the moment any polarization effects or losses in the medium.<sup>4</sup>

Given equation 23, the problem of determining the detectability of EAS-initiated ionization columns reduces to that of determining the effective RCS  $\sigma_b$  for a given choice of operating radar frequency, and the noise power of the specific radar in use. The noise power is given by  $P_N = kT_{sys}\Delta f$ , where  $T_{sys}$  is the system noise temperature,  $k$  is Boltzmann's constant, and  $\Delta f$  the effective receiving bandwidth, assumed here to be matched to the transmitting bandwidth.

**Pulse compression radar.** Almost all modern pulsed radar systems now use what is known as *pulse compression*, a method which allows the receiver bandwidth, and thus the noise power, to be minimized (cf. Wehner 1987). Pulse compression is typically implemented by effectively dispersing a band-limited pulse with an initial bandwidth  $\Delta f_0 = (\Delta t_0)^{-1}$  through a filter, transforming it into a frequency chirp which spans the original bandwidth, but now has a duration  $\Delta t \gg \Delta t_0$ . The receiver then uses an inverse filter to de-disperse the received pulse. The effective bandwidth is thus  $\Delta f = (\Delta t)^{-1}$ , but the range resolution  $\Delta R \propto \Delta t_0$  of the full bandwidth is recovered.

**CW radar.** Continuous wave radar systems which transmit at 100% duty cycle, can derive range information by using frequency- or phase-encoded waveforms to uniquely tag the detected echoes to a particular time segment of the transmitted waveform. Processing of the received sig-

nal typically involves mixing with a reference signal, which transforms different ranges to different frequencies, followed by detection in a filterbank. The effective bandwidth is then determined by the bandwidth of the frequency channels used.

For simplicity we will assume a pulsed radar system here and in what follows.

Combining the noise power equation above with equation 23, the signal-to-noise ratio (SNR) of the received power is

$$\frac{P_r}{P_N} = \sigma_b P_t \eta \frac{G^2 \lambda^2}{(4\pi)^3 R^4} \frac{1}{k T_{sys} \Delta f}. \quad (24)$$

Evaluating equation 24 for a nominal choice of parameters gives the SNR per received radar pulse per square meter of RCS:

$$\begin{aligned} \frac{S}{N} &= 3.3 \left( \frac{\sigma_b}{1 \text{ m}^2} \right) \left( \frac{P_t}{1 \text{ kW}} \right) \left( \frac{\eta}{0.1} \right) \left( \frac{G}{10} \right)^2 \\ &\times \left( \frac{\lambda}{3 \text{ m}} \right)^2 \left( \frac{R}{10^4 \text{ m}} \right)^{-4} \left( \frac{T_{sys}}{10^3 \text{ K}} \right)^{-1} \left( \frac{\Delta t}{10 \text{ } \mu\text{s}} \right). \end{aligned} \quad (25)$$

We note that the reference values chosen here represent a modest radar system; in particular the peak power of 1 kW is easily attained by current standards, and the directivity  $G \simeq 10$  (beam size  $\sim 1$  sr) represents a relatively low-gain antenna. The system temperature  $T_{sys} = 1000$  K is realistic for 100 MHz ( $\lambda = 3$  m) however, since the brightness temperature of the sky is quite high at these frequencies.

Radar systems also routinely use repetitive pulsing to increase SNR, which then grows roughly as  $N_p^{1/2}$  where  $N_p$  is the number of pulses that are averaged. In the case of an EAS, the number of pulse repetitions is limited by the free electron lifetime, with large uncertainty. For the shortest possible electron lifetimes, it is unlikely that repetitive pulsing can provide much improvement in SNR, but for lifetimes of order 1 ms, repetitive pulsing could provide substantial improvements in SNR.

<sup>4</sup>This equation is also derived strictly under conditions where the received radiation is in the far-field, that is, where  $R > 2D^2/\lambda$  where  $D$  is the largest projected dimension of the scattering target. In our case, this is not generally satisfied, since the length of the ionization columns can be tens of km. However, we have already accounted for these Fresnel zone effects by limiting our analysis to the first Fresnel zone as noted above.

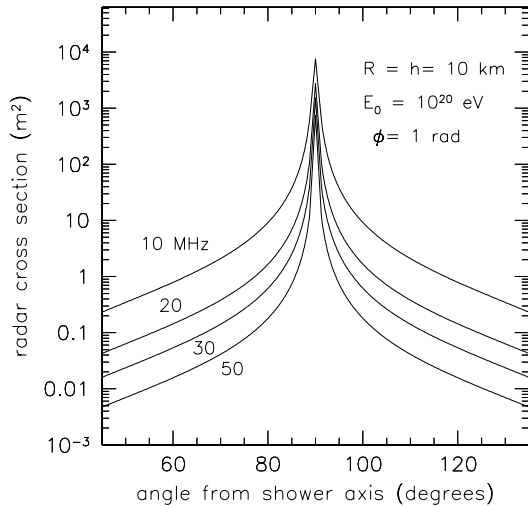


Fig. 6.— Radar cross section over a range of angles centered on normal incidence (at  $90^\circ$ ) for an air shower with  $E_0 = 10^{20}$  eV, at a distance of 10 km, at radar wavelengths 30, 15, and 10 m. Results are based on the thin wire approximation. The polarization of the incident wave has been taken to be 1 radian with respect to the shower axis; thus these RCS values should apply on average to random relative orientations.

We now consider in detail the expected RCS for EAS ionization columns in the various density regimes that were introduced above.

#### 4.1. Low-frequency/overdense case

At radar frequencies below the plasma frequency of the ionized core of the EAS, the RCS is comparable to that of a metal cylinder, as noted above, with a radius of  $r_c$  and a length equal to that of the Fresnel zone. Based on the analytical shower model used above and the results in Fig. 2, the critical radius at a given wavelength and EAS cascade energy  $E_0$  can be empirically

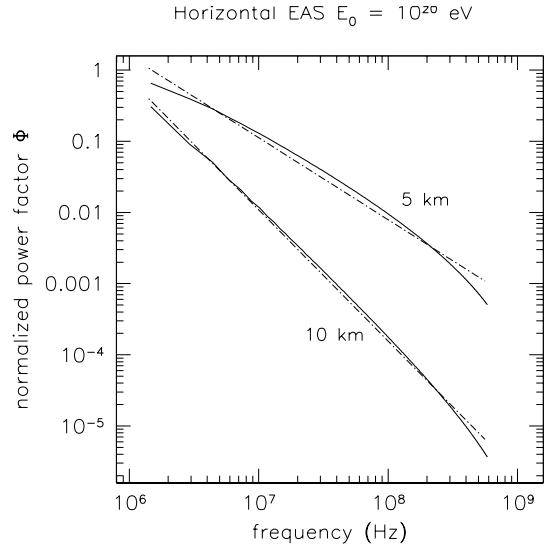


Fig. 7.— Normalized power loss factor due to loss of coherence for two horizontal  $E = 10^{20}$  eV showers at heights of 5 and 10 km.

approximated by

$$\frac{r_c}{\lambda} = \frac{1}{30} \left( \frac{f}{10 \text{ MHz}} \right)^{-0.75} \left( \frac{E}{10^{20} \text{ eV}} \right)^{0.85} \text{ m.} \quad (26)$$

It is evident from this result that for frequencies above 10 MHz, and for all but the highest EAS energies considered here,  $r_c \ll \lambda$  and we can use the thin wire approximation discussed above.

In Fig. 6 we show results for radar cross sections of the first Fresnel zone for a shower of  $E_0 = 10^{20}$  eV, for three different frequencies, for a range of angles centered on normal incidence, and a polarization angle of 1 rad with respect to the shower axis. The cross section at normal incidence is greatly enhanced due to the specular reflection at that angle. We can empirically express the maximum cross section for this case as

$$\sigma_b^{od}(10 \text{ km}) = 2.2 \times 10^3 \left( \frac{f}{30 \text{ MHz}} \right)^{-1.45} \times \left( \frac{E}{10^{20} \text{ eV}} \right)^{0.44} \left( \frac{R}{10 \text{ km}} \right) \text{ m.} \quad (27)$$

It is clear from this analysis<sup>5</sup> that overdense showers will show very large cross sections when the reflection is nearly specular. However, as seen in Fig. 6, the cross sections decrease rapidly for non-specular reflections. This behavior will be seen to contrast sharply with the case of underdense scattering, to be treated below. Any consideration of the detectability of a particular shower must account for both contributions to the cross section.

In the analysis above we have also ignored the additional contribution due to the partially coherent scattering of the much larger volume of underdense plasma outside of  $r_c$ . This region could have refractive effects on the incoming radiation. In an appendix we treat this issue in some detail and show that it produces a negligible effect for the showers under consideration here.

#### 4.2. High-frequency/underdense case

When either the frequency is high enough or the ionization density low enough that there is effectively no region of the column where the critical density obtains, the radar return is due to Thomson scattering of the free electrons in the column, modulated by the phase factor associated with the physical extent of the ionized region as described in equation 8 above.

We have made numerical estimates of the effective cross section for a restricted set of cases here, with the methods described in more detail in an appendix. Here we summarize the results.

##### 4.2.1. Normal incidence

For the case of radar observations at normal incidence to the shower, the near constancy of

---

<sup>5</sup>Here the linear increase of the cross-section with shower impact parameter  $R$  is due to the fact that the size of the first Fresnel zone grows with distance. In fact, although we have used the length of the Fresnel zone  $L_F$  as the characteristic length of the “thin wire” portion of the shower, the actual length of this region is likely to be much longer than  $L_F$ .

the ionization density along the track allows us to estimate the frequency dependence of the phase factor via a Fast Fourier transform (FFT) of the two dimensional ionization distribution in a plane transverse to the track. We have taken advantage of this feature to make numerical estimates of the frequency-dependent behavior of the phase factors at normal incidence.

Note that the requirement of normal incidence for the radar rays interrogating the shower is not as restrictive as it might seem. For example, consider a horizontal shower whose maximum is at a range of  $R_1$  from the radar transmitter/receiver system, and whose axis is inclined an angle  $\theta$  with respect to the ray that joins the radar source and the shower maximum. Under these conditions, the radar system can still interrogate the shower along a ray that intersects the shower at normal incidence at a distance  $R_1 \cos \theta$  from the shower maximum.

Thus a horizontal shower at 10 km altitude, with 15 km range to its maximum, and inclined at  $\theta = 60^\circ$  will have a ray that intersects it at normal incidence at a longitudinal distance along the shower of 7.5 km from shower maximum, at a range of 13 km, where the ionization line density is still  $\sim 60\%$  of its maximum value. Thus the corresponding acceptance solid angle over which these results apply is not negligible, if the beam of the radar system is not too restrictive in solid angle.

Fig. 7 shows our estimates of the frequency dependence of the phase factor for two horizontal showers at altitudes of 5 and 10 km, for  $E_0 = 10^{20}$  eV. The phase factor depends strongly on both frequency and shower altitude. The frequency dependence is due to loss of coherence as noted above, and the altitude dependence arises from the change in Moliere radius to smaller values at lower altitudes. We have also investigated the behavior at other energies in this regime and found these results to be insensitive to energy over the range  $10^{18} - 10^{21}$  eV. For the two cases

shown we have included fitted power laws

$$\Phi(f; 5 \text{ km}) = 0.114 f_{10}^{-1.15}$$

$$\Phi(f; 10 \text{ km}) = 1.13 \times 10^{-2} f_{10}^{-1.84} .$$

Here  $f_{10}$  is the radar frequency in units of 10 MHz. These relations are individually accurate to about 20% over the range from 10 MHz to 0.3 GHz.

Given the power loss associated with the phase factor, the total cross section is then estimated by summing the cross sections of the individual volume elements over one Fresnel zone of the track, by analogy to the overdense case, and multiplying by the overall phase factor for the radar frequency and shower altitude.

Evaluating this modified cross section for its energy and frequency dependence, we derive an empirical expression for the case of a horizontal EAS at altitude of 10 km

$$\begin{aligned} \sigma_b^{ud}(10 \text{ km}) &= 175 \left( \frac{f}{30 \text{ MHz}} \right)^{-1.84} \\ &\times \left( \frac{E}{10^{20} \text{ eV}} \right)^{1.9} \left( \frac{R}{10 \text{ km}} \right) \text{ m}^2. \end{aligned} \quad (28)$$

and similarly for an altitude of 5 km:

$$\begin{aligned} \sigma_b^{ud}(5 \text{ km}) &= 1400 \left( \frac{f}{30 \text{ MHz}} \right)^{-1.15} \\ &\times \left( \frac{E}{10^{20} \text{ eV}} \right)^{1.9} \left( \frac{R}{10 \text{ km}} \right) \text{ m}^2. \end{aligned} \quad (29)$$

These relations should be valid out to ranges of several tens of km. At the highest energies and lowest frequencies the underdense case may not obtain, but these estimates will then provide a lower limit on the RCS.

#### 4.2.2. Oblique angles

For shower angles away from normal incidence, it is necessary to consider all of the individual scattering contributions of the electrons over the entire volume of the shower, and to treat

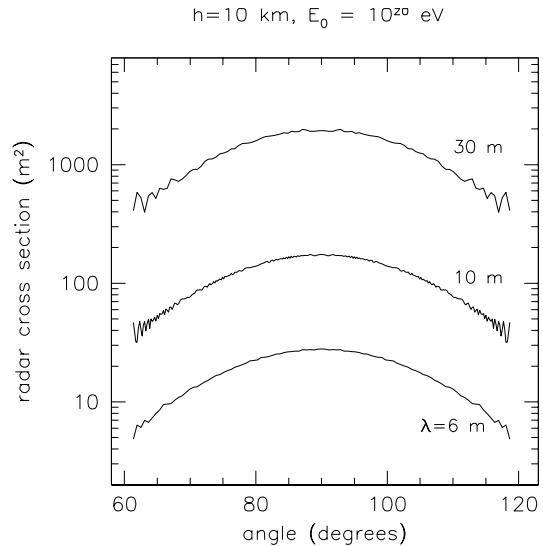


Fig. 8.— Radar cross section over a range of angles centered on normal incidence (at  $90^\circ$ ) for a horizontal air shower with  $E_0 = 10^{20}$  eV, at an altitude of 10 km, at radar wavelengths 30, 10, and 6 m. Results are based on numerically integrating the contributions of all of the individual volume elements of the shower.

the pulse echo behavior explicitly. We discuss this in detail in an appendix. We have numerically estimated the integrated RCS for several wavelengths at a distance of 10 km to display some of the characteristics of the angular dependence.

The results of this are shown in Figures 8 and 9. We have plotted the total RCS as a function of angle over about 1 radian around normal incidence, for a horizontal shower at heights 10 and 5 km and energy  $10^{20}$  eV, and several different radar wavelengths. The dependence on angle is quite different from the overdense case where specular reflection is important; here, the cross section has an approximately Gaussian profile with angle, with a FWHM of order  $30^\circ$ . The fairly steep wavelength dependence is also independent of angle over this range. Thus the empirical relations derived in the previous section can



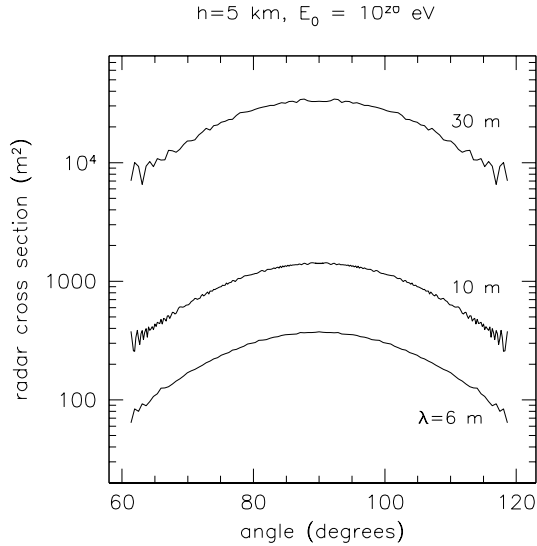


Fig. 9.— Similar to previous figure, with shower altitude of 5 km.

be used with appropriate factors for the angle of incidence shown here.

We caution here that the angular dependence of the RCS at distances that are much greater than the length of the shower is probably not accurately reflected by these results. We have not yet derived a general analytical treatment of the behavior for large distances, but we note that the methods described in the appendix allow for numerical estimates to be made at any distance.

### 4.3. Caveats

We note that, due to self-imposed limitations of scope, a number of effects have not been treated in our analysis. We list several of these here.

**Geomagnetic effects.** We have neglected geomagnetic charge separation in the shower development. Although this is an important effect in determining the detailed shower structure, it depends greatly on the shower direction with respect to the magnetic field. Its effect on the RCS

would also depend on the angle of observation and the treatment of this complex interaction is beyond our scope at present.

### Landau-Pomeranchuk-Migdal (LPM) effect.

We have neglected the LPM effect in the showers considered here. This effect, which retards the initial growth of the shower, is important at the energies discussed and should be accounted for in a more detailed treatment. However, it affects primarily shower which interact initially through the electromagnetic rather than the hadronic channel, and thus there are still many EAS at these energies for which the approximation used is still accurate.

### Secondary Fresnel zone echoes.

For simplicity we have only treated the echo from the primary Fresnel zone here. In fact, for the high SNR case, many distinct echoes may be detected from successive Fresnel zones, and these will certainly add significantly to the understanding of any detected shower. On the other hand, for underdense showers that are not observed near normal incidence, the time spread of the return will also tend to decrease the instantaneous SNR. Such effects are important in understanding the response of a radar system to the wide variety of possible EAS directions and relative angles and will need to be explored further in any real application.

### Near vertical EAS.

For convenience we have analyzed a horizontal air shower, but such showers are of general interest, since such highly-inclined showers imply very deep initial interactions and are thus a possible signature of neutrino primaries. For more typical showers with small zenith angles, the Moliere radius changes significantly during the shower development and complicated the analysis considerably. Generalization of our analysis to EAS at all angles is best done with a full numerical simulation. Preliminary results of such a simulation (D. Bergman

2000, pers. comm.) do not show significant differences in the ionization profiles, and still show a tight core in the radial ionization density.

**Pulse smearing by the shower.** Note that our results for the underdense case above apply in a general way only to non-pulsed radar, since the superposition implied by the Fourier transforms assumes that each Fourier component extends spatially out to dimensions that are much larger than the shower column. For pulses whose compressed time scale is physically shorter than the time-projected thickness of the ionization column of a shower, we must explicitly account for the behavior of the individual pulse echoes from different portions of the shower. However, the effective RCS corresponding to the integrated power of the echo is still described by our analysis to first order.

A general consideration of the complications arising from the pulsed nature of the radar are beyond our scope at present but must be included in any detailed estimate of the pulsed radar echo behavior. In the appendix we describe a method developed to deal with pulsed-radar reflections, and we utilize this method in some later results.

**Plasma resonance effects.** We have treated the underdense case in a simplified way which neglects the possibility of plasma resonance effects. Such effects are in fact seen in meteor echoes (Poulter & Baggaley 1977) and can play an important role in enhancing the RCS, and in producing more complex time structure in the radar return.

## 5. Discussion

In the previous sections we have presented evidence that EAS ionization columns are well within the range of VHF radar detection for cascade energies above  $\sim 10^{18}$  eV. Now we turn to a discussion of the applicability of this approach to present efforts at detection and characterization

of such EAS. To establish a basis for comparison, we first outline the capabilities of fluorescence detector systems, to which EAS radar detection, if possible, would be most similar.

**Fluorescence detector capabilities.** The most capable present fluorescence detector system is the High Resolution Fly’s Eye system in Utah (Abu-Zayyad et al. 1999) operating for several years now in “monocular” mode, and now beginning to come on line with stereo-mode operation, using a pair of telescope clusters separated by 12.6 km. HiRes uses about 1 photomultiplier per square degree of focal-plane sky coverage, with 2-3 m aperture low-resolution optical telescopes used as the light collectors.

HiRes can detect events out to 20-25 km, although at this distance the effects of aerosols increase the uncertainty of the measurements. To achieve reasonable precision in the measurement of 6 shower parameters (three geometric and three associated with the energy and shower development) requires typically a minimum of about 20 photomultiplier pixel hits in monocular mode, giving at this level an energy resolution of  $\sim 25\%$  and precision of about  $30 \text{ gm cm}^{-2}$  in the position of shower maximum (P. Sokolsky 2000, pers. comm.). Significant improvement in the precision of these measurements is expected once the stereo mode comes into full operation (Abu-Zayid et al. 1999). Observation efficiency for any Fluorescence detector is limited to about 10% since the observations can only be made on clear, moonless nights. The total acceptance aperture for HiRes is expected to be about  $6000 \text{ km}^2 \text{ sr}$  in the region of  $10^{20}$  eV shower energy.

### 5.1. Standalone EAS radar system.

Here we consider what type of radar system would be required to produce EAS measurements that can be compared to those expected from HiRes.

Because of the issues of interference rejection,

a standalone EAS radar system would almost certainly have to be constructed with multiple stations configured to both transmit and receive, with pulse encoding such that each station would be sensitive to pulses produced by the other stations. Bistatic radar cross sections of EAS will vary only modestly from the monostatic RCS values treated here. Global synchronization of the stations to several tens of ns or less is routine with the Global Positioning System, particularly with the disabling of Selective Availability (SA) of the high precision GPS codes.

To optimize the signal-to-noise ratio of the detected echoes, we wish to operate at the lowest frequency that is practical from considerations of background noise, including ionospheric noise from daytime operation. Although lower frequency operation may be possible, we choose here to consider only frequencies above about 30 MHz. In the HF-VHF regime the effective system noise temperature for a remote site (distant from urban noise sources) can be written as (Skolnik 1986):

$$T_{sys} = 2.9 \times 10^6 \left( \frac{f}{3 \text{ MHz}} \right)^{-2.9} \text{ K} \quad (30)$$

which yields  $T_{sys} = 3600\text{K}$  at 30 MHz.

Assuming that each station receives an echo from its own as well as all others in an array of  $M$  transmit/receive stations, there are  $M + M(M - 1)/2$  complex measurements for each combined pulse of the  $M$  stations. For six EAS parameters to be fitted, the minimum number of stations required is  $M = 3$  (giving 6 total geometric ranges and echo amplitudes), assuming that the measurements are independent. Given that there will be some covariance of the measurements, and requiring that the fit be well-constrained, at least 4 or 5 stations will be needed, giving 12-20 ranges and amplitudes. Additional closure-delay (or triangle) measurements number  $M(M - 1)(M - 2)/6$ , and will provide an extra 4-10 independent constraints for the  $M = 4$ ,  $M = 5$  cases, respectively. However,

these latter constraints apply only to the geometry, which is typically well-constrained in any case, and not the echo amplitude. Addition of dual-polarization capability, which is not uncommon in radar systems, would double the number of measurements.

### 5.1.1. Radar data types.

The measured data can be characterized as follows:

**Range data & shower angle.** The time delay to the leading edge of the echo at each station will provide the range from the transmitter to the receiver. The ranges can be measured typically to a precision of roughly the compressed pulse width divided by the SNR. For a SNR=10, and a compressed pulse width of 250 ns, the range resolution is below 10 m.

A complete determination of the angular resolution possible using radar is beyond our scope, but simple arguments can show that a set of 4 or 5 stations should provide reasonable estimates of the track direction. A schematic view of the geometry associated with the range measurements for a pair of stations is shown in Fig. 10. Here the stations 1 and 2 measure leading-edge ranges  $R_1$  and  $R_2$  to separate portions of the shower at along-track positions  $s_1, s_2$  with respect to shower maximum. The stations are separated by a baseline  $B_{12}$  which is not generally parallel to the shower track. Let a vector  $\mathbf{n}$  bisect the baseline and the shower segment from  $s_1$  to  $s_2$ . The shower direction can then be characterized by angles  $\alpha$ , which measures the rotation of the shower track around the axis  $\mathbf{n}$  with respect to the projected baseline, and  $\beta$  which measures the angle between the shower and  $\mathbf{n}$ .

It is evident from Fig. 10 that changes in  $\beta$  will under most conditions produce first order changes in the range values, eg.

$$\sigma_\beta \sim \frac{\sigma_R}{|s_2 - s_1|} \quad (31)$$

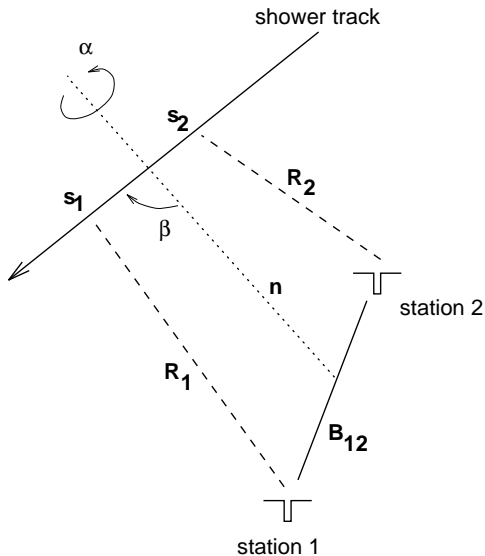


Fig. 10.— A schematic of the range constraints on shower angles provided by a pair of radar stations 1 and 2, separated by baseline  $B_{12}$ . See text for details.

where  $\sigma_R$  is the mean range error and  $\sigma_\beta$  the resulting angular resolution in  $\beta$ . Since for tracks that are primarily transverse to the baseline  $B_{12}$ , we have  $|s_2 - s_1| \sim B_{12}$ , then baselines of order 5 km or more with range errors of  $\sim 10$  m will give angular resolution in  $\beta$  of order several mrad, or about  $0.1^\circ$ .

Changes in  $\alpha$  for a pair of stations under typical expected detection geometry do not give first order effects in range, and are thus more problematic. Because a change in  $\alpha$  corresponds to a kind of “torsion” mode of the range constraints (using a rigid-rod analogy), the error in  $\alpha$  for a two station solution is likely to generally behave as

$$\sigma_\alpha \sim \frac{\sqrt{2R} \sigma_R}{|s_2 - s_1|} \quad (32)$$

which applies most directly to the case where  $\alpha \ll 1$ . For example, for  $R = 20$  km,  $\Delta s = 5$  km, and  $\sigma_R = 10$  m, we have  $\sigma_\alpha \simeq 7^\circ$ , much lower precision than can be achieved in air flu-

orescence detectors. We note however that the addition of more radar stations, with the inclusion of bistatic ranges and multiple polarization measurements should rapidly improve the precision as more constraints are added, but further estimates are beyond our scope at present.

**Echo amplitude data.** The echo amplitude is more difficult to interpret. For underdense showers, the echo amplitude is directly proportional to the number of electrons present, and thus is similar to fluorescence detectors in terms of its ability to estimate the number of ions within a certain region of the track. However, since the radar echo may be spread out over a band of different ranges, determination of the contributing portion of the shower for each portion of the returned echo at each receiving station is a clearly more complicated problem than that faced by fluorescence detectors, which rely on imaging precision to solve this problem. However, since the geometric parameters of the shower track are easily separable via the range data, the resulting amplitude of the leading edge of the return can be attributed unambiguously to the portion of the ionization column that is nearest to the receiving station. By thus reconstructing a profile of these prompt received amplitudes at their relative positions along the geometric track, the profile of the shower development can be extracted.

For overdense showers, the radar echos may show anomalously high strength compared to expectations based on an underdense echo. In this case, interpretation of the data may rely on distinguishing these two cases on an event-by-event basis. Estimates of the effective conductivity of the plasma can then still yield the electron content of the shower.

In either of these cases, the amplitude data, although not as straightforward to interpret at that of fluorescence measurements, still provides the type of calorimetry of an EAS that is necessary to determine the shower energy. This is a feature that particle counter arrays cannot match

in detail, and it sets apart the fluorescence detection and potential radar detection techniques from other methods.

### 5.1.2. Duty Cycle.

Perhaps the most interesting feature of radar as a potential EAS detection approach is the possibility of much higher duty cycle observations over detection volumes comparable to those of fluorescence detectors. In principle a radar system is not limited to night operation, and suffers very little attenuation from clouds or aerosols. Although operation in the presence of lightning within the detection volume might produce some spurious events, avoiding operation in periods of lightning would cost at most a few percent of the livetime.

The largest uncertainty in efficiency is probably due to the free electron lifetime, since if this is very short, it may be difficult to ensure adequate pulse repetition frequency to detect all showers. And although radar propagation is unaffected by aerosols and clouds, the free electron lifetime is not immune to variations in these components of the atmosphere, and in practice they may be important limitations to the efficiency. In addition, the presence of the sun above the horizon will increase the system temperature somewhat, especially near solar maximum, and this will act to increase the detection threshold for daytime operation.

## 5.2. SNR Budget for a standalone EAS radar system

In Figure 11 we show a plan view of the geometry of a radar array using both monostatic and bistatic detection of an EAS, here shown with 4 stations at 3-5 km spacing, providing 10 ranges and 10 pulse amplitudes. Here we describe the parameters required of each transmit/receive station to satisfy the needs of the array described.

If we assume that we require an energy threshold of  $10^{19}$  eV out to a range of 20 km, the im-

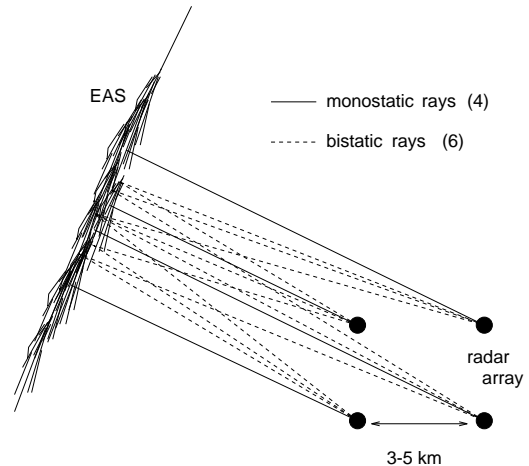


Fig. 11.— An array geometry for a possible standalone EAS radar detection system. Each of the 4 stations has both transmit & receive capability, and can distinguish the signals from the other stations as well.

plied RCS for the underdense case is  $\sim 2 \text{ m}^2$  at this energy. The Fresnel zone length at this range is about 250 m for a shower at 10 km altitude, corresponding to about  $10 \text{ g cm}^{-2}$  along the track. Using a commercial VHF radar system, it is straightforward to achieve 60 kW peak power and pulse repetition rates of 10-50 kHz for 10  $\mu\text{s}$  pulses. The sky brightness temperature will lead to a system temperature of  $T_{sys} = 3600 \text{ K}$  at 30 MHz as noted above. Since we wish to be sensitive to as large a volume as possible, we use an antenna with a broad beam (thus corresponding to a low gain). A suitable system is a vertical monopole or discone system (Balanis 1997) which provides good  $2\pi$  azimuthal coverage from  $5^\circ$  to about  $50^\circ$  elevation, giving an overall gain of  $\sim 3$  with respect to an isotropic antenna. We also assume here a somewhat pessimistic overall transmit/receive efficiency of  $\eta = 0.05$ , and a single pulse echo (no pulse averaging) to account for possible rapid decay of the free electron population.

Table 1: SNR budget for one station of a possible EAS standalone radar system.

Parameter	value	$\pm$ dBm
<b>Received Power</b>		
<i>Received Power</i>	$\sigma_b \eta P_t G^2 \lambda^2 \times (4\pi)^{-3} R^{-4}$	
Peak transmit power	60 kW	77.8
Pulse duration	10 $\mu$ s	...
chirp bandwidth	3 MHz	...
Number of repetitions	1	0.0
Antenna gain	3	9.54
wavelength	10 m	20.0
$\sigma_b$ at $E = 10^{19}$ eV	3.8 m <sup>2</sup>	5.8
range to EAS	20 km	-172.0
xmit/rev efficiency	0.05	-13.0
$(4\pi)^{-3}$	$5.04 \times 10^{-4}$	-33.0
<b>Received power</b>		-104.9 dBm
<b>Noise power</b>		
<i>Noise power</i>	$kT_{sys}\Delta f$	
Boltmann's constant	$1.38 \times 10^{-20}$ mWK <sup>-1</sup> Hz <sup>-1</sup>	-198.6
System temperature	3650 K	35.6
effective bandwidth	100 kHz	50.0
<b>Noise power</b>		-113.0 dBm
<b>SNR</b>	6.4	8.0 dB

Using these assumptions we show the SNR budget, in dBm (decibels referenced to 1 milliwatt) in Table 1. This budget corresponds to a single monostatic or bistatic pulse measurement in the array. The resulting SNR of 6.4 provides a range resolution of 34 m at a 30 MHz operating frequency, using a chirp bandwidth of 10% (3 MHz in this case).

We can also estimate the rate of shower detection as a function of energy. To do this we estimate that the acceptance solid angle of the system is  $\sim 1$  sr, based on the RCS within  $10^\circ$  of the peak values. This is significantly lower than that of a fluorescence detector, and reflects the rapid decrease in the RCS as the angle of incidence moves away from the normal to the shower

axis. We also consider only the RCS for showers at 10 km altitude, although showers at lower altitudes will have significantly higher cross sections in general. The integral number of events seen above a given energy  $E_{thr}$  is given by

$$Q(E_{thr}) \simeq \pi R_{eas}^2 \eta_{obs} T \Omega I(E \geq E_{thr}) \quad (33)$$

where  $\eta_{obs}$  is the observing efficiency,  $T$  the observation duration,  $\Omega \simeq 1$  is the effective solid angle, and

$$I(E \geq E_{thr}) \simeq \left( \frac{E_{thr}}{10^{19} \text{ eV}} \right)^{-2} \text{ km}^{-2} \text{ sr}^{-1} \text{ yr}^{-1} \quad (34)$$

is the integral cosmic ray spectrum at these energies. Here the maximum range for detection is determined by inverting equation 4 above, which yields:

$$R_{eas}(\text{km}) = 82 \left( \frac{S/N}{10} \right)^{-1/3} \left( \frac{E_{thr}}{10^{20} \text{ eV}} \right)^{0.63} \times \left( \frac{P}{1 \text{ kW}} \right)^{1/3} \left( \frac{\eta}{0.1} \right)^{1/3} \left( \frac{G}{10} \right)^{2/3} \times \left( \frac{T_{sys}}{1000 \text{ K}} \right)^{-1/3} \left( \frac{\Delta t}{10 \mu\text{s}} \right)^{1/3}. \quad (35)$$

This relation is approximately valid to energies of order  $10^{20}$  eV, where the detection range is  $\sim 80$  km. Beyond this range, the minimum beam elevation is such that it exceeds the initial assumption of 10 km shower altitude, and the detection efficiency as a function of shower altitude must be more explicitly addressed. However, this exercise highlights the large potential detection area for a radar system.

In Figure 12, we plot the expected event rate per year for 80% observing efficiency, which is achievable with a fully operational system. Here the assumed minimum  $SNR = 6.0$ . Also plotted with respect to the right axis is the effective aperture, in km<sup>2</sup> sr, for the same assumptions.

It is evident from this analysis that EAS detection by radar certainly merits further investigation as a high-duty cycle alternative to existing EAS detection systems. Although it is

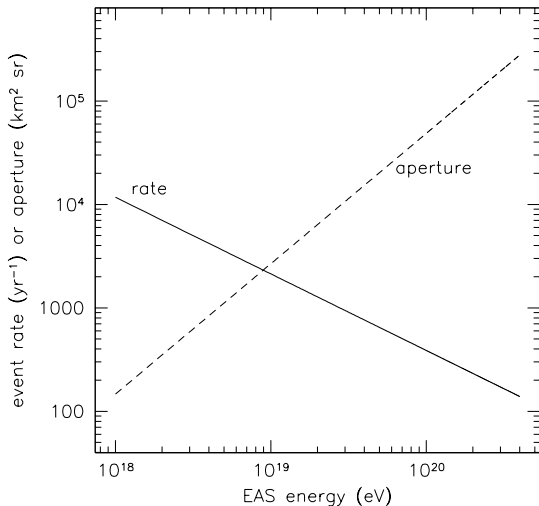


Fig. 12.— The expected event rate detected at a SNR=6 for the standalone EAS radar system described in the text and table 1. The effective aperture corresponding to this rate is also plotted.

not a competitive technique at lower energies, it appears that this approach may have significant benefits for detection of EAS at the highest energies. Although it may not be able to compete with fluorescence detection in its ultimate accuracy in the estimation of shower parameters, a system which utilizes a trigger provided by an existing particle detector array such as the Auger Observatory could potentially gain valuable complementary information on daytime events where fluorescence information cannot be obtained.

## 6. Conclusions

We have demonstrated that, using standard models for the average behavior of extensive air shower development, the resulting ionization appears straightforward to detect using radar techniques in the VHF frequency range (30–100 MHz), for primary energies greater than about  $10^{18}$  eV. We estimate that a relatively modest

ground-based system could provide information on EAS that is comparable to that available from other techniques, and may do so with a much higher duty cycle and potentially a larger effective aperture. The approach requires no new technology, making use of standard radar equipment and detection techniques, and may thus also provide a low-cost alternative to existing methods.

We thank an anonymous referee who provided a very valuable critique. We thank Douglas Bergman, George Resch, Pierre Sokolsky, Paul Sommers, David Saltzberg, and Trevor Weekes for useful discussion and comments. This research has been performed at the Jet Propulsion Laboratory, California Institute of Technology, under contract with the National Aeronautics and Space Administration.

## REFERENCES

- Antoni, T., et al., 2000, *Astroparticle Phys.*, in press, (also arXiv:astro-ph/0004233).
- Appleton, E. V., and Piddington, J. H., 1937, *Proc. Roy. Soc. A*, 164, 467.
- Balanis, C. A., 1997, *Antenna Theory*, 2nd edition, (New York: Wiley & Sons).
- Baltrusaitis, R. M., Cady, R., Cassidy, G. L., Cooper, R., Elbert, J. W., Gerhardy, P. R., Ko, S., Loh, E. C., Salamon, M., Steck, D., & Sokolsky, P., 1985, *NIM A240*, 410.
- Blackett, P. M. S., and Lovell, A. C. B., 1940, *Proc. Royal Soc. (London) Ser. A*, 177, 183.
- Bourdeau, M. F., et al., 1980, *J Phys. G: Nucl. Phys.* 6, 901.
- Buonsanto, M., Sipler, D. P., Davenport, G. B., & Holt, J. M., 1997, *J. Geophys. Res.* 102 (17), 267.
- Capelle, K.S., Cronin, J.W., Parente, G., & Zas, E., 1998, *Astropart. Phys.* 8, 321.
- Colwell, R. C., and Friend, A. W., 1936, *Phys. Rev.* 50, 632.

- Dawson, B.R. et al., 1997, Proc. 25th International Cosmic Ray Conf., Durban, OG 10.6.16.
- Dolezalek, H., 1982, in Hand. Chem. Phys., ed. Weast & Astle, F-172.
- Gallagher, J. W., Beaty, E. C., Dutton, J., and Pitchford, L. C., 1983, J. Phys. Chem. Ref. Data, 12(1), 109.
- Greenhow, J. S., 1952, Proc. Phys. Soc. B, 65, 169.
- Gregory, A., and Clay, R. W., 1982, in Hand. Chem. Phys., ed. Weast & Astle, F-175.
- Greisen, K., 1965, in Prog. Cosmic Ray Physics vol. III, J.G. Wilson ed., (North Holland: Amsterdam) 1.
- Guérard, C. K., et al. 1998, Proc. Workshop Front. Astroph. & Part. Physics, Vulcano, Sicily.
- Hanbury Brown, R., & Lovell, A. C. B., 1962, *The Exploration of Space by Radio*, 2nd ed., (New York: Wiley).
- Hightower, C. H., Brown, T., & Soon, N. Y., 1993, Proc. of the IEEE Nat. Radar Conf., 6.
- Jones, J. & Jones, W. 1991, Planet. Space Sci. 19(9), 1289.
- Jones, W., 1991, Planet. Space Sci. 1991, 19(9), 1283.
- Kaiser, T. R., & Closs, T., 1952, Phil. Mag. 43, 1.
- Kamata, K., & Nishimura, J., 1958, Suppl. Progr. Theoret. Phys. 6, 93.
- Kraus, J. D., 1988, *Antennas*, 2nd ed., (New York: McGraw-Hill).
- Krizmanic, J. et al., 1999, Proc. 26th Int. Cosmic Ray Conf., eds. Kieda, Dingus & Salamon, (Univ. Utah: Salt Lake City) vol 2, 388.
- Lidga, M. G. H., 1950, Bull. Amer. Meteor. Soc., 31, 279.
- Lidga, M. G. H., 1956, J. Atm. Terr. Phys. 9, 329.
- Lovell, A.C.B., & Clegg, J. A., 1948, Proc. Phys. Soc. 60, 491.
- Matano, T., Nagano, M., Suga, K., and Tanahashi, G., 1968, Can. Journ. Phys. 46, S255.
- Miles, V. G., 1952, Nature 170.
- Poulter, E. M., & Baggaley, W. J., 1977, Journ. Atmos. Terrest. Phys. 39, 757.
- Rosner, J. L., and Wilkerson, J. F., 1997, appendix to the proposal for the Auger Air Shower Array; hep-ex/9702008.
- Rossi, B. B., 1964, *Cosmic Rays*, New York: McGraw-Hill).
- Sahr, J. D., and Lind, F. D., 1997, Radio Sci. 32(6), 2345.
- Scarsi, L. et al., 1999, Proc. 26th Int. Cosmic Ray Conf., eds. Kieda, Dingus & Salamon, (Univ. Utah: Salt Lake City) vol 2, 384.
- Seaton, M., 1959, MNRAS 119, 81.
- Segre, E., 1977, *Nuclei and Particles*, 2nd ed., (Reading, MA: Benjamin/Cummings).
- Skolnik, M., 1990, *Radar Handbook*, (New York: McGraw-Hill), 2nd ed.
- Stalio, R. et al. 1999, Proc. 26th Int. Cosmic Ray Conf., eds. Kieda, Dingus & Salamon, (Univ. Utah: Salt Lake City) vol 2, 403.
- Sovers, O. J., Fanselow, J. L., and Jacobs, C. S., 1998 Rev. Mod. Phys. 70(4), 1393.
- Suga K., 1962, Proc. Fifth Interamerican Seminar Cosmic Rays, 2, XLIX.
- Thomas, L. 1972, Journ. Atmos. Terr. Phys. 33, 157.
- Watson Watt, R. A., Bainbridge-Bell, L. H., Wilkins, A. F., and Bowen, E. G., 1936, Nature 137, 866.
- Watson Watt, R. A., Wilkins, A. F., and Bowen, E. G., 1936, Proc. Roy. Soc. A, 161, 181.
- Wehner, D. R., 1987, *High Resolution Radar*, (Norwood, MA: Artech House).



Williams, E. R., Geotis, S. G., and Bhattacharya, A., B., 1989, *J. Atm. Sciences*, 46(9), 1173.

Zhou, Q. H., and Kelley, M. C., 1997, *Journ. Atm. & Sol.-Terr. Phys.* 59(7), 739.

## A. Appendix 1: Numerical Evaluation of RCS for the underdense case

To estimate the RCS for the underdense regime of an EAS ionization column, we need to evaluate the individual contributions of the scattering electrons and the phase of the resulting scattered fields. As noted in section 2 above, under certain conditions this is equivalent to determining the Fourier transform of the electron distribution. Here we describe the basis for this conclusion and provide details of the methods used for numerical evaluation of the RCS under these circumstances.

### A.1. Geometry of the problem

The geometry for this evaluation is shown in Fig. A13. Here we let  $\mathbf{R}$  represent the vector distance from the origin  $O$  (at the radar transmitter/receiver) to the position of shower maximum. We choose the  $x - y$  plane to be coincident with the plane containing the axis of the shower and  $\mathbf{R}$ . Within the ionization column itself, we use cylindrical coordinates  $\rho, \phi, z_1$  to calculate the proper ionization density at position  $P$  with respect to the position of shower maximum;  $\mathbf{r}' = (\rho, \phi, z_1)$  is the vector separation of  $P$  from shower maximum. The vector joining the origin to  $P$  is denoted as  $\mathbf{r}$ . The angle between the shower axis and  $\mathbf{R}$  is denoted  $\theta$ .

Given these definitions, we find

$$|\mathbf{r}|^2 = \rho^2 + z_1^2 + R^2 + 2R(\rho \cos \phi \sin \theta - z_1 \cos \theta) \quad (\text{A1})$$

which expresses the distance to an arbitrary point in the ionization column as a function of

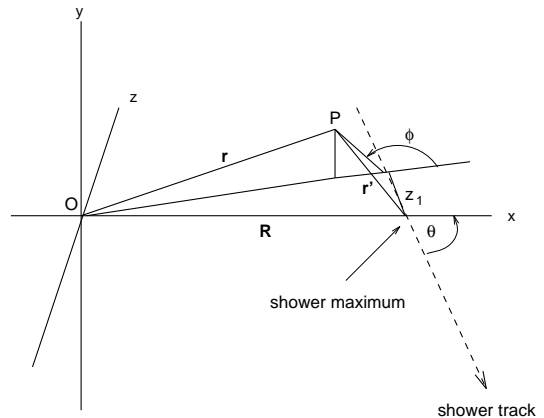


Fig. A13.— The geometry for numerical evaluation of the summed radar cross section of an ionization column for the case of oblique angle of incidence. The radar transmitter/receiver is at the origin  $O$ , and the angle of the track is  $\theta$  with respect to the direction from the origin to shower maximum  $R$ . The vector to the position  $P$  in the ionization column that is being evaluated is  $\mathbf{r}$ , and the vector separation of  $P$  from the position of shower maximum is  $\mathbf{r}'$ .  $\phi$  is the azimuthal angle of  $P$  in cylindrical coordinates with respect to the shower axis.

the distance to shower maximum, the local cylindrical coordinates of the point, and the angle of obliquity  $\theta$  of the shower.

### A.2. Scattered field

The electric field that is incident at  $P$  can be written as

$$U_{inc} = U_{tr} G_{tr} e^{i\omega t} \frac{e^{i\mathbf{k}\cdot\mathbf{r}}}{|\mathbf{r}|} \quad (\text{A2})$$

where  $U_{tr}$  is the magnitude of the transmitted field,  $G_{tr}$  is the transmitter gain factor (as defined in the main text),  $k = 2\pi/\lambda$ , and  $\mathbf{r}$  is defined in Fig. A13. Assuming that  $\mathbf{k}$  and  $\mathbf{r}$  are parallel (that is, neglecting the effective dielectric behavior of the underdense plasma in the column), the received field from a small volume of

This 2-column preprint was prepared with the AAS L<sup>A</sup>T<sub>E</sub>X macros v4.0.

electrons  $n_e dV$  which scatter coherently is then given by

$$dU_{rcv} = U_{inc} \sqrt{\sigma_T} n_e dV G_{sc} e^{i\omega t} \frac{e^{i\mathbf{k}_{sc} \cdot \mathbf{r}_{sc}}}{|\mathbf{r}_{sc}|} \quad (\text{A3})$$

where  $G_{sc}$  is the effective gain of the electron scattering process ( $G_{sc} = 1$  for isotropic scattering),<sup>6</sup> and  $\mathbf{k}_{sc}$ ,  $\mathbf{r}_{sc}$  are the wavevector and radial vector of the scattered wave. In this case we have  $\mathbf{k}_{sc} = -\mathbf{k}$  and  $\mathbf{r}_{sc} = -\mathbf{r}$ , and thus

$$dU_{rcv} = U_{tr} G_{tr} G_{sc} \sqrt{\sigma_T} n_e dV e^{i\omega t} \frac{e^{2i\mathbf{k} \cdot \mathbf{r}}}{|\mathbf{r}|^2} \quad (\text{A4})$$

which displays the expected radial dependence of the field (equivalent to a  $r^{-4}$  dependence in received power), and also the additional factor of two in the spatial phase which is due to the two-way trip of the radiation.

If we assume for the moment that the time variation of the field is steady-state, we can drop the time dependence, and integrate over the volume of the shower to yield the total received field strength, assuming that the transmitted beam is larger than the dimensions of the shower. If we also assume that the distance from the shower is large enough that  $|\mathbf{r}| \approx |\mathbf{R}|$ , then we have

$$R^2 U_{rcv} = U_{tr} G_{tr} G_{sc} \sqrt{\sigma_T} \int_V n_e(\mathbf{r}) e^{i\mathbf{q} \cdot \mathbf{r}} d^3\mathbf{r} \quad (\text{A5})$$

which shows (taking  $\mathbf{q} = 2\mathbf{k}$ ) that the received field is proportional to the Fourier transform of the electron density distribution.

### A.3. Normal incidence

Under conditions where the pulse is incident on the ionization column at normal incidence, and if we assume that the ionization column is essentially constant along its longitudinal length,

<sup>6</sup>For Thomson scattering,  $G_{sc} \simeq 1.6$  corresponding to electric dipole emission. However, this response is complicated in any real plasma by a number of effects, and we have assumed  $G_{sc} = 1$  for all cases considered here.

the received field becomes proportional to the two-dimensional Fourier transform of the cross-sectional electron density, times the length of the Fresnel zone  $L_F$  (defined as the length over which the scattered fields are in phase):

$$R^2 U_{rcv}|_{\theta=0} = U_{tr} L_F G_{tr} G_{sc} \sqrt{\sigma_T} \int_A n_e(\mathbf{r}) e^{i\mathbf{q} \cdot \mathbf{r}} d^2\mathbf{r}. \quad (\text{A6})$$

We have numerically evaluated this using Fast Fourier transform techniques, since the area  $A$  over which this is done is of order  $A = \pi r_m^2$  and the number of  $\lambda_{min}/8$  cells in the grid is  $64A/\lambda_{min}^2$ , where we have assumed  $\lambda_{min} \sim .5$  m, giving a  $(2^{13})^2$  grid. The result of the FFT can be normalized to provide a frequency-dependent phase factor, which we have plotted in Fig. 7 above.

### A.4. Pulsed radar & the time-projected RCS

In the previous analysis we have assumed a steady-state incident field (which corresponds to carrier-wave or CW radar). However, in our analysis of section 4, we assumed that the radar is pulsed, and in fact pulsed radar is preferable to achieve the kind of time resolution required in this application. For the overdense case, the analysis presented in section 4 is adequate, since we are considering reflections from a localized source at the critical radius of the ionization column. Also, for normal incidence, the reflections from the first Fresnel zone arrive closely in phase and can be treated without explicitly accounting for the pulse echo behavior.

When we allow for oblique shower angles, however, the concept of the Fresnel zone loses its usefulness, and the received echo comes from the entire volume of the shower and is thus significantly spread out in time. We require a method of treating the behavior of a discrete pulse under these conditions.

The approach we have followed is intuitively simple: we first produce a time-projected profile of the electron density; that is, we calculate the

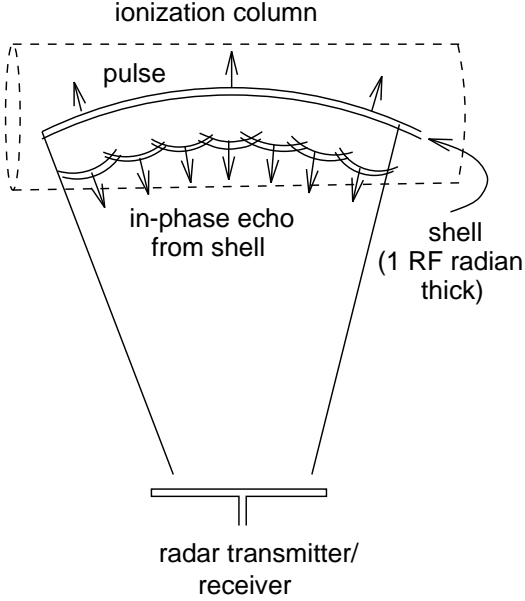


Fig. A14.— Illustration of the geometry that gives rise to the concept of the time-projected radar cross section. The ionization column can be divided into radial shells such that all of the electrons that scatter the incoming radar are in phase (to within a radian) within the shell.

round-trip time associated with the global phase of each of the contributing differential volume elements of the scattering electrons

$$t_i = \frac{\lambda}{2\pi c} \mathbf{q} \cdot \mathbf{r}_i . \quad (\text{A7})$$

Here  $t_i$  is the round-trip time for the  $i$ th volume element at location  $\mathbf{r}_i$ . If we consider all of the volume elements for which  $t_i = t_j$  within a specified interval  $\Delta t \leq \omega^{-1}$ , then we define a shell at distance  $r = t/2c$  with a thickness of 1 radian of phase at the radar angular frequency  $\omega$ . This is depicted in Fig. A14.

Summing all of the contributing elements in this shell gives the time-projected square root of the total cross section at that phase:

$$Y(t)\Delta t = \sqrt{\sigma_T} \int_{r-t/4c}^{r+t/4c} n_e(\mathbf{r}) d^3\mathbf{r} . \quad (\text{A8})$$

Once  $Y(t)$  is determined for a given radar wavelength, shower angle and energy, and distance, then the pulse response of the ionization column is determined by convolving the electric field of the pulse profile with  $Y(t)$ , and squaring the result. If the pulse is defined to have unit amplitude, then the resulting convolution can be expressed as an effective radar cross section for use in equation 4.

For example, if the pulse is assumed to be a  $\delta$ -function in time, the resulting convolution  $\Upsilon(t)$  is

$$\Upsilon(t) = \int_{-\infty}^{\infty} Y(t')\delta(t-t')dt' = Y(t) \quad (\text{A9})$$

and the received power is then proportional to  $|Y(t)|^2$ . For other pulse profiles we numerically evaluate the convolution explicitly, and take the maximum of the resulting profile to be the effective radar cross section.

In Fig. A15 we show an example of the square of  $Y(t)$ , giving the time-projected cross section calculated according to the manner described here. In each case the time bins correspond to a radian of angular phase according to the wavelength indicated, and the value for each bin is estimated according to equation A8. The profile in this case shows a characteristic rapid rise on its leading edge, reflecting the rise in cross-sectional ionization density of the nearest portion of the shower. The more slowly falling trailing edge is due to the contributions from portions of the shower further away.

We note that  $Y(t)$  defined in this way is analogous to a Green's function for the time response of the system. It can be used in this manner to evaluate arbitrary radar pulse shapes, for a given EAS energy and direction. For extremely broad-band radar systems, the effective RCS values will begin to approach those of  $Y(t)$ . For more narrow-band radar pulses, the convolution of the field oscillations with  $Y(t)$  will act to partially cancel and the effective RCS will decrease.

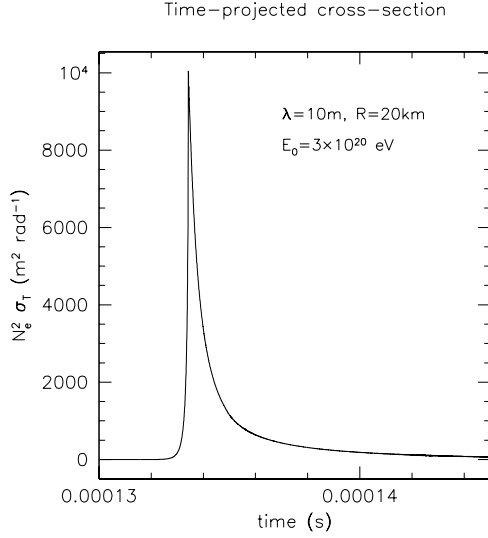


Fig. A15.— The square of the function  $Y(t)$ , which gives the time-projected total radar cross section, for an ionization column produced by a shower with  $E_0 = 3 \times 10^{20}$  eV, for  $\lambda = 10$  m, at a distance of 20 km. The time axis is windowed around the arrival time of the round trip travel time.  $Y(t)$  may be thought of as a kind of Green's function time response of the ionization column to a sharp radar pulse, with a magnitude that is proportional to the square root of the RCS at a given pulse phase.

## B. Appendix 2: Refractive effects of the plasma halo

The refractive index of a plasma is given by Spitzer (1962) in the quasilongitudinal approximation by

$$n = \left[ 1 - \left( \frac{\nu_p}{\nu} \right)^2 \right]^{1/2} \quad (\text{B1})$$

where we have assumed that the frequency of the radiation is well above the electron gyrofrequency in the earth's magnetic field ( $\sim 840$  kHz). In this case the phase delay of the radiation after propagating a distance  $l$  through the plasma is

given as (cf. Sovers et al. 1998):

$$\Delta_{pd} = -q/\nu^2 \quad (\text{B2})$$

where the variable  $q$  here represents the column density of the electrons integrated along the ray path:

$$q = \frac{cr_0}{2\pi} \int n_e dl \quad (\text{B3})$$

where  $r_0$  is the classical electron radius and  $c$  is the speed of light. The negative phase delay, or phase advance given above is characteristic of propagation in a plasma. More appropriate for consideration here is the group delay, obtained by differentiating  $\phi = \nu \Delta_{pd}$  with respect to frequency

$$\Delta_{gd} = q/\nu^2 \quad (\text{B4})$$

which constitutes a net additive delay that increases at lower frequencies. Numerically, this delay has the value

$$\Delta_{gd} = 1.34 \times 10^{-3} \chi_e / \nu^2 \text{ sec} \quad (\text{B5})$$

where  $\chi_e$  is the electron column density in  $\text{e}^- \text{cm}^{-2}$

Integrating the electron densities in the halo of a  $10^{20}$  eV shower along a radial path from outside the shower down to a radius of 1 m and then back out again (to approximate the radar ray path) yields  $\chi_e \simeq 4 \times 10^8 \text{ e}^- \text{cm}^{-2}$ , and the corresponding delay at 30 MHz is 0.6 ns, or about  $6^\circ$  of RF phase. A group delay of this order will have a negligible effect on the received power compared to the geometric phase factors. At lower frequencies, such as 10 MHz, the group delay is an order of magnitude larger, but the induced RF phase lag is still only  $\sim 20^\circ$ . Thus it appears that the refractive effects of the radial plasma halo can be ignored to first order for the EAS ionization columns considered here.

Similar analysis of ray-path deviation along chords in the outer halo (due to the gradient in the plasma density) shows that the refraction is not significant until the chords approach within

several m of the EAS core for the highest energy showers. Thus although it is important to include such effects in any final calibration of parameters estimated by radar measurements, they do not appear to bear significantly on the detectability of the showers.